

# Vision-based Deformation Measurement for Pile-soil Testing

Kun Zhou<sup>1</sup>, Linhua Chen<sup>1</sup>, Shanshan Yu<sup>2</sup>

<sup>1</sup>Economy and Technology Research Institute, State Grid Hunan Electric Power Company, Changsha, Hunan, 410004, China

<sup>2</sup>School of Civil Engineering, Southeast University, Nanjing, Jiangsu, 211100, China

Corresponding author: *Shanshan Yu*, [1454431046@qq.com](mailto:1454431046@qq.com)

**Abstract.** Image measurement technology has been widely used in monitoring the deformation of the soil field around the pile with its advantages of no damage, no contact, full-field measurement, no added quality and high sensitivity. But there are few researches on image-based bearing deformation measurement of the pile. Through an indoor pile-soil semi-model test, the rigid body displacement and load-bearing deformation of a new type of prefabricated steel tube pile foundation under horizontal load was measured based on image features. In this study, the concept of optical extensometer is first applied to the measurement of local average strain of a non-uniform deformed structure. Based on an improved feature point tracking algorithm SURF-BRISK, non-contact measurement of tiny strain of pile body is realized. In addition, based on DIC technology, this study also obtained the progressive development of displacement field of soil around pile. The above work fully reflects the non-contact convenience and full-field richness of the optical measurement method compared with the traditional measurement method.

## 1. Introduction

Deformation measurement analysis in model test of geotechnical engineering occupies an important position to study the geotechnical properties. Model test has been necessary means to build, check and improve the soil constitutive model which provide important references [1-2] for pile foundation, foundation treatment, tunnel excavation, slope support, underground caverns and road building, etc. At present, there are two ways to measure soil deformation. One is contact method such as laying displacement sensors and drawing grid lines on the mode. The contact method has many defects. First, the effect of the dense tracing marks is not easy to determine. Second, the tracing markers could not meet the requirement of high strain gradient. Third, the measuring points of displacement must be determined in advance. Fourth, the number of measuring points is limited, which obviously fails to meet the requirements of qualitative and quantitative research on the micro-mechanical characteristics of rock and soil and the characteristics of full-field deformation. In fact, sand particles have different colours and can form natural speckle images with different grayscale under the irradiation of ordinary light sources. That is the noncontact method using the optical technique to

measure the deformation field of the whole area. In recent years, the extensive application of digital image technology and the rapid development of computer hardware provide technical and theoretical guarantees for vision-based deformation field measurement of the geotechnical model [3-4]. Based on DIC technology, the optical extensometer is realized by using the camera to track and locate the mark on the specimen surface [5]. As a new method to test the mechanical properties of materials, it has been widely used [6]. Kumr et al. [7] used an optical extensometer to determine the optimal thickness of a micro specimen. Dubos et al. [8] applied the 3D video extensometer to the experimental study on the size effect during the high purity metal sheet forming process. Wang wei et al. [9] applied optical extensometer to real-time strain measurement of low-dimensional materials. The concept of optical extensometer can be used to accurately measure the small displacement at variable range, which thoroughly solves the technical problem that the extensometer must be mechanically connected with the specimens, which will easily cause permanent damage to the extensometer in case of large displacement and accidental fracture. Nevertheless, 2D DIC has always been restricted to nominal planar

surfaces that subjected to mainly “in-plane” deformations but out-of-plane motions are ubiquitous in experiments. So it is significant that even though very small out-of-plane motion could bring in large deviation in strain measurement. In order to improve the precision, a telocentric lens can be chosen [10]. Another choice is stereovision 3D DIC system setup developed in the early 1990s [11–13]. The out-of-plane motions turn not to adverse the effect that greatly influences the strain results as in 2D DIC. However, cross-camera subset matching and the procedure of calibration are complex, and as the telocentric lens, the strain accuracy of 3D DIC measurement is also limited to about 100  $\mu\epsilon$ . [14] used a special experimental setup called “correction sheet” to eliminate the virtual strain induced by out-of-plane motions.

Different from existing research methods, this paper is based on feature matching algorithm to track the real-time pixel coordinates at both ends of certain standard distance. Unlike template matching methods, feature tracking technology requires stable interest points which can be detected and effectively matched. Feature point tracking process consists of three steps: detection, description, and matching. During the last decade, a variety of feature detectors including Scale-Invariant Feature Transform (SIFT) [15], Speeded-Up Robust Features (SURF) [16], and Features from Accelerated Segment (FAST) [17], as well as descriptors including SIFT, SURF, Harris corner detection [18], Binary Robust Independent Elementary Features (BRIEF) [19], Oriented FAST and Rotated BRIEF (ORB) [16], Binary Robust Invariant Scalable Keypoint (BRISK) [21], and Fast Retina Keypoint (FREAK) [18] have been developed.

The features detected by the SIFT algorithm are located more precisely in space and scale. The algorithm can detect abundant feature points [19], but the process of feature point extraction takes a lot of time because of the huge computation required, while SURF is twice as fast. SURF is much more time saving than SIFT. Bekele et al. [20] compared the performance of five feature descriptors BRIEF, ORB, BRISK, FREAK and SIFT, finding that BRISK delivered the highest accuracy and maximum number of optimal match point pairs among the five binary feature descriptors. In addition, random sampling consistency (RANSAC) can be adopted to filter out incorrect matching point pairs. For the case of obvious rotation and scale change, RANSAC can effectively rule out some wrong matching pairs, however, it is not very effective for small rigid-body translation.

This paper is organized as following. Part 1 explains the research background including application requirements of optical measurement technology in soil experiment, development of optical extensometer, and feature point tracking algorithms concerned in this paper. Part 2 will interpret relevant theories about DIC, SURF-BRISK and the working principle of the new matching strategy, Part 3 is the application of optical methods to a pile soil experiment including soil deformation field measurement based on DIC and pile average strain measurement based on SURF-BRISK. Part 4 is the results. Part5 is the conclusions and discussion. This study fully reflects the potential of the application of optical non-contact measurement to the pile –soil load test under horizontal load.

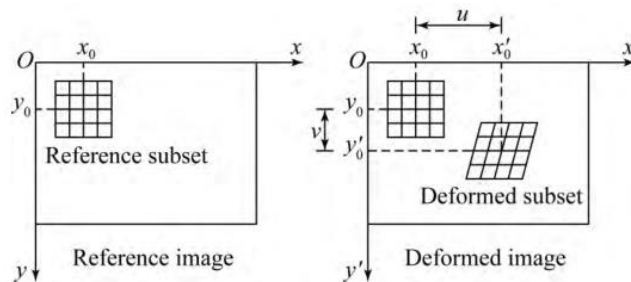


Fig. 1. Principle of two-dimensional digital image

## 2. Correlation method of deformation measurement based on image

### 2.1 Basic principles of 2D DIC

The basic principle of two-dimensional DIC is shown in Fig 1. Assuming that the gray level of the same point on the object surface remains unchanged before and after the deformation, the small adjacent region of each point is called a sub-region or template. By using the gray scale matching method of sub-region image. Select the rectangle in the reference image  $f(x,y)$  with center point  $(x_0,y_0)$ . Search for the target sub-region matching the gray level of the reference sub-region in the

distorted image  $g(x',y')$ . In the search process, a certain search strategy should be followed and a preselected correlation function should be followed. The common standardized cross-correlation function is as follows:

$$C = \frac{\sum_{i=-M}^M \sum_{j=-N}^N f(x_i,y_j)g(x'_i,y'_j)}{\sqrt{\sum_{i=-M}^M \sum_{j=-N}^N f^2(x_i,y_j)} \cdot \sqrt{\sum_{i=-M}^M \sum_{j=-N}^N g^2(x'_i,y'_j)}} \quad (1)$$

The target sub-region that makes the correlation function reach to the extreme value will be the target deformation sub-region. By calculating coordinate difference between calculation point  $(x_0,y_0)$  and deformation zone center  $(x'_0,y'_0)$ , the displacement in the x and y

directions of u and v can be obtained.

## 2.2 Improved SURF-BRISK

Combined SURF-BRISK is used as the feature tracking algorithm in this study, and in this way, advantages from both algorithms are retained including the most matching point pairs and the highest matching precision compared to common algorithms. SURF-BRISK algorithm generates stable edge points through Hessian matrix. Following this, a transformation image from the original image is required. In SURF, the transformation image is formed by the approximation of the Hessian matrix determinant of each pixel point in the original image. Assuming that the estimated values of filtering in the direction of  $x$ ,  $y$  and  $xy$  after convolution are  $D_{xx}$ ,  $D_{yy}$  and  $D_{xy}$  respectively, the approximate formula of determinant is as follows:

$$\det(\text{Happrox}) = D_{xx}D_{yy} - (0.9D_{xy})^2 \quad (2)$$

As feature points must be scale independent, it is necessary to build a scale space pyramid through Gauss filter before constructing the Hessian matrix. In SURF, the size of the image remains unchanged but the Gauss blur size of different octave layers is different, and the Gauss template scale of images in the same octave is also different. The next step in this process is to refine the feature points by comparing the determinant value of one point with the other 26 points. The extreme point obtained is still rough and needs to be precisely located. The SURF algorithm uses 3D linear interpolation to obtain sub-pixel feature points. Based on the scale and the coordinate of a feature point detected by SURF, a neighbourhood sampling mode is established by BRISK. To avoid the influence of image gray aliasing on sampling, Gauss functions of difference standard deviations  $\sigma_i$  is used to smooth each sampling point  $P_i$ . The proportional to the distance between the points on each concentric circle is  $\sigma_i$ . The small blue circle represents the sampling position, and the large red circle radius is the standard deviation of the Gauss kernel corresponding to the sampling position. The local gradient is:

$$g(p_i, p_j) = (p_j - p_i) \times \frac{I(p_j, \sigma_j) - I(p_i, \sigma_i)}{p_j - p_i^2} \quad (3)$$

where  $I(p_j, \sigma_j)$  and  $I(p_i, \sigma_i)$  are the gray values of the sample point after smoothing. The main direction of feature point k is:

$$g_x = \frac{1}{L} \times \sum_{(p_i - p_j) \in L} g_x(p_i, p_j) \quad (4)$$

$$g_y = \frac{1}{L} \times \sum_{(p_i - p_j) \in L} g_y(p_i, p_j) \quad (5)$$

where L is the set of long-distance sampling point pairs. In order to make sure the feature points are scale invariant and rotation invariant, the feature point is rotated at a certain angle  $\alpha = \arctan 2(g_x, g_y)$ , and then compared with the short sample point set S. The binary descriptor b is:

$$b = \begin{cases} 1, & I(p_j^\alpha, \sigma_j) > I(p_i^\alpha, \sigma_i), \forall (p_j^\alpha, p_i^\alpha) \in S \\ 0, & \text{the other} \end{cases} \quad (6)$$

Feature matching is based on binary descriptors, that is, to establish the relationship between feature points reflecting the same physical location. Hamming distance is used to measure the similarity of feature descriptors in this paper. If the two descriptors  $b_1 = x_1x_2 \dots x_{512}$  and  $b_2 = y_1y_2 \dots y_{512}$ , Hamming distance is:

$$D(b_1, b_2) = \sum_{i=1}^{512} (x_i \oplus y_i) \quad (7)$$

KNN matching method is adopted with K=2 and the threshold value of the nearest neighbour and sub-neighbour ratio is 0.65. This paper improves SURF-BRISK by selecting the target feature points before calculating Hamming distance and matching. The selection criteria is based on the maximum deformation prediction of structure in the form of search radius.

This idea originates from the small and easily estimated deformation with little scale change in field testing. It is understood that the distance between the pixel coordinates of the successful matching point pair is within a certain upper limit. This paper proposes a matching strategy suitable for a large structure with small deformation, as shown in the Fig.2. The pixel coordinates of feature points waiting for being matched in the reference image is  $(X_o, Y_o)$ , the pixel coordinates of one target feature point in deformed image is  $(X_i, Y_i)$ , and the search radius  $R = A$  which means the maximum displacement can never be more than A. The target point of which the pixel distance d is less than R is potentially the best matching feature point, or it will be eliminated and the same step for the next feature point will begin. This process is repeated to gather a set of target feature points. The next step is to obtain the binary descriptor of the target feature points based on the BRISK descriptor. This new strategy prevents redundant calculation and reduces many wrong matching pairs, which is beneficial to displacement measurement.

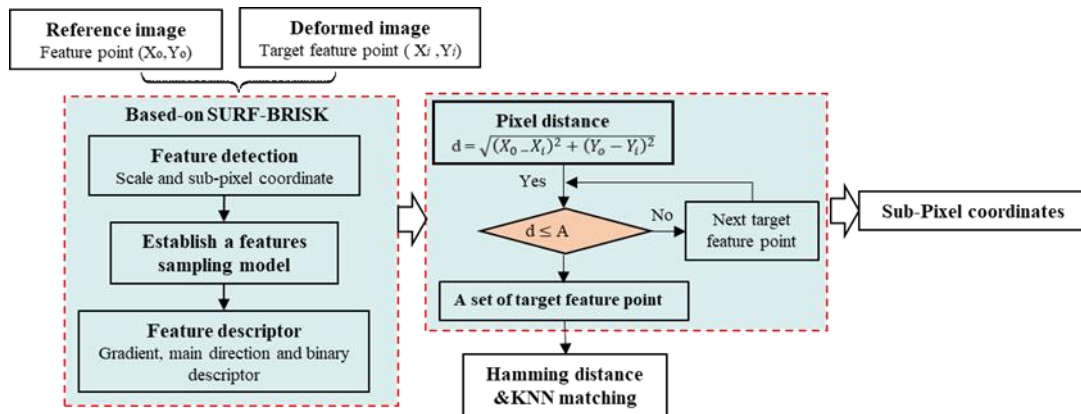


Fig. 2. Improved Features tracing theories

### 2.3 Optical extensometers

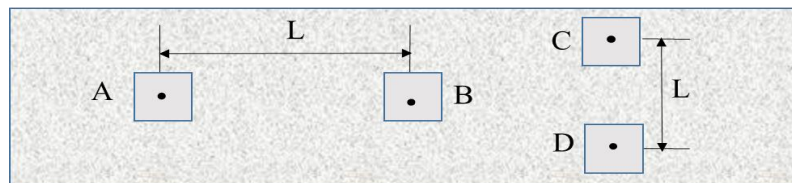


Fig. 3. Schematic diagram of optical extensometer

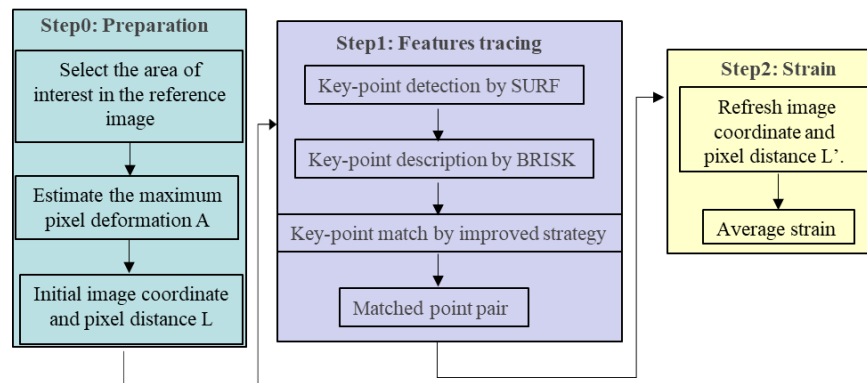


Fig. 4. Flow chart of strain calculation

Four feature points A, B, C and D are selected as the standard distance points on the surface of the specimen (Fig.3). AB and CD are respectively the optical extensometers for the axial and transverse strain of the specimen. Since the measurement principles of the two are the same, only the measurement principles of axial strain are introduced here. The steps are as shown in Fig.4. An image is collected as an initial reference before loading.

Initial pixel distance between A and B is the standard distance  $L = \sqrt{(X_A - X_B)^2 + (Y_A - Y_B)^2}$ , images are collected for calculation after the pile moved horizontally and the pixel distance comes to be  $L'$ , then the average strain of this standard distance is

$$\varepsilon = \frac{L' - L}{L} \quad (8)$$

## 3. Pile-soil testing

### 3.1 Experimental setup

As shown in Fig. 5 the length and width of the steel box are 1000mm, the height is 1300mm, and the thickness is 5mm. For the convenience of the camera to track the movement of the pile and soil, sliding groove is reserved on both sides of the box, and 8mm thick tempered glass with thickness of 8mm is used to replace a side wall of the steel box. In case of the wet sand contaminate the inner wall of glass, resulting in measurement blind area, wet sand needs to be pre-dried. It should be noted that the half pile model must be be placed close to the glass and stabilized before sand filling. While filling the sand special attention should be paid to prevent the sand flow into the region

between the thickness position of steel pipe and glass wall. The depth of the steel pipe pile in soil is 800mm, the outside diameter is 100mm, and the wall thickness is 2mm. To facilitate loading, the length of free segment of the pile is 300mm. The pile body was uniformly and continuously laid with 8 strain gauges, each of which are 10cm long. As shown in Fig. 6, an industrial camera with a resolution of 2048pixel × 2048pixel and a 50mm fixed lens with a focal length of 50mm were used. In order to eliminate the effect of glass reflecting, two 50w LED lights were set up symmetrically.

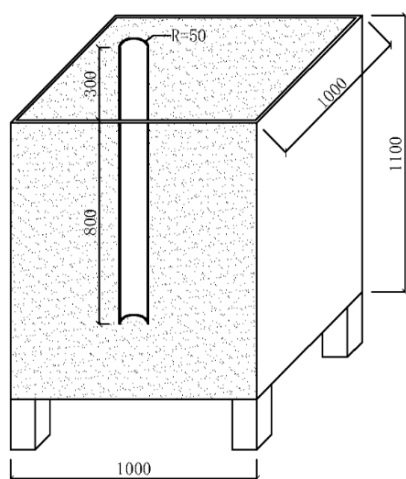


Fig. 5. Schematic diagram of pile-soil model

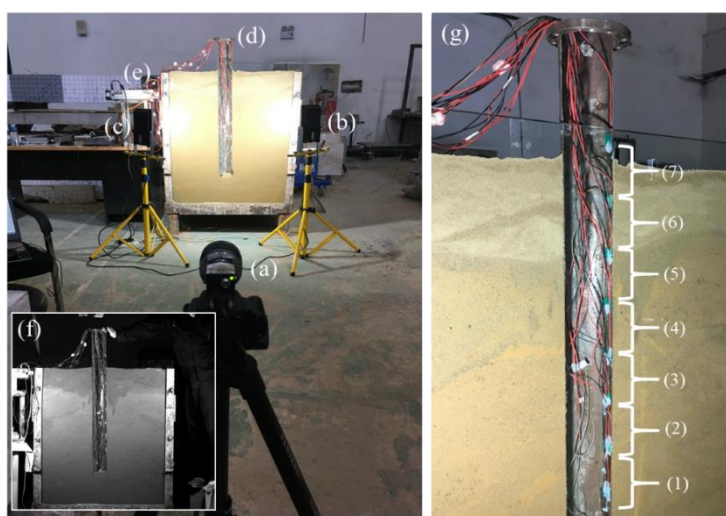


Fig. 6. Schematic diagram of experimental equipment (a) Camera (b) rightlight (c) left camera (d)pile (e) acquisition instrument (f) image for optical analysis (g) strain gauges deployment

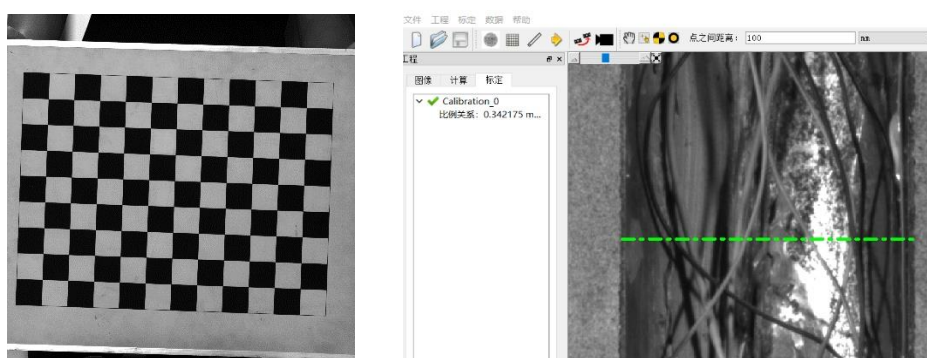


Fig. 7. Schematic diagram of Camera calibration.(a) calibration board (50mm) (b) scale factor calibration interface

### 3.2 Distortion and scale factor

Optical distortion exists between the actual image of the object point on the image surface and the ideal image point, causing the measurement error. This paper only considers

the main radial distortion and the tangential distortion. Acquisition calibration board (Fig.7.(a)) with different posture, and use Zhang camera calibration method [21], its

process is to calculate the homology matrix, camera intrinsic parameters using two constraint equations based on the orthogonality of the rotation matrix, extrinsic parameters, and then distortion parameters by L-M nonlinear iteration with initial value 0.

In order to transform pixel displacement into physical

displacement, this study used the known size, namely the diameter of steel pipe pile 100mm, to calibrate the scale parameter  $s$  (about 292pixel) in the image.  $s=0.342\text{mm/pixel}$  (Fig.7(b)).

## 4. Deformation results

The top pile is subjected to a cyclic horizontal load. This paper defines the positive direction of horizontal displacement and vertical displacement in Fig.8. In general, only the sand near the top pile has obvious displacement field. The total displacement cloud diagram Fig.8(a) shows that with greater displacement load to the right, there is a gourd-shaped displacement field near the right side of the pile and a half U-shaped displacement field near the left top pile. According to the cloud map of horizontal displacement Fig.8(b), when the pile moves to the left, the

### 4.1 Evolution of soil displacement field

horizontal displacement maximum occurs near the left top side of the pile body. While when the pile moves to the right, the sand slightly lower than the top surface of soil body moves most obviously. The most interesting should be vertical displacement cloud map Fig.8(c). It is not difficult to see that when sand is squeezed by piles, the sand body near the pile body has no vertical displacement, while a similar concentric displacement field in shapes is generated slightly away from the pile body. This was unexpected.

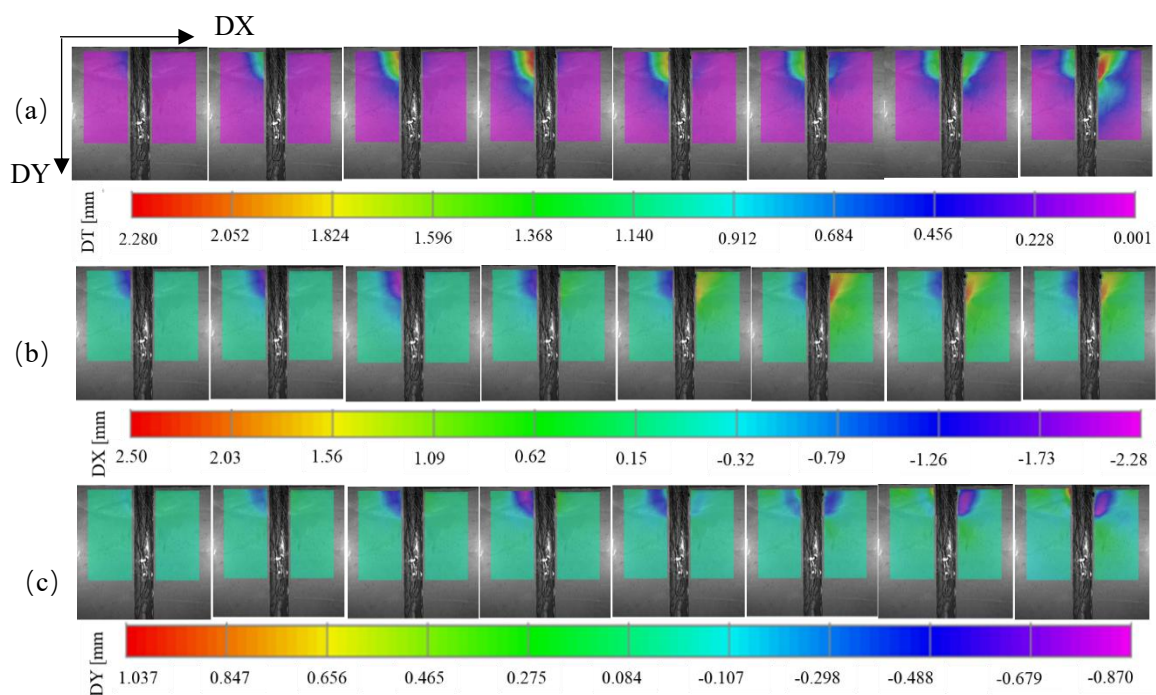


Fig. 8. Cloud picture of soil displacement (a) total displacement DT (b) horizontal displacement DX(c) Vertical displacement DY

### 4.2 Deformation of the steel pile

In this paper, the main steps to get the average strain of each section of pile body are as following. First, select the area of interest at both ends of the strain gauge. Second,

track the feature points in the area adopting SURF-BRISK algorithm. Third, determine the feature points for calculation and export the pixel coordinates. Forth, get the

pixel distance of the corresponding points before and after deformation, and then deduce the average strain. Considering the limited precision of the field of view, four sections (corresponding to strain gauge (4), (5) and (6)) with larger strain are measured in this paper (Fig.9). The results are as following.

It can be found in Fig.10 and Fig.11 that the trend of strain measured by strain gauge and the camera show good consistence. The average difference value between them is about  $35\mu\epsilon$  and the maximum strain difference does not exceed  $65\mu\epsilon$ .

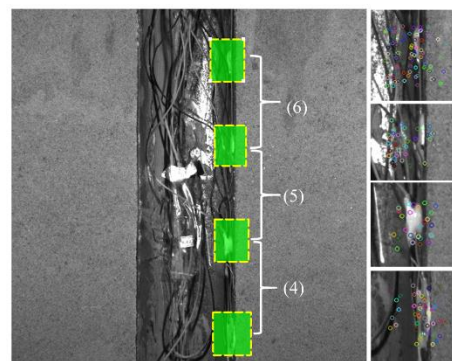


Fig. 9. Pile surface features tracing

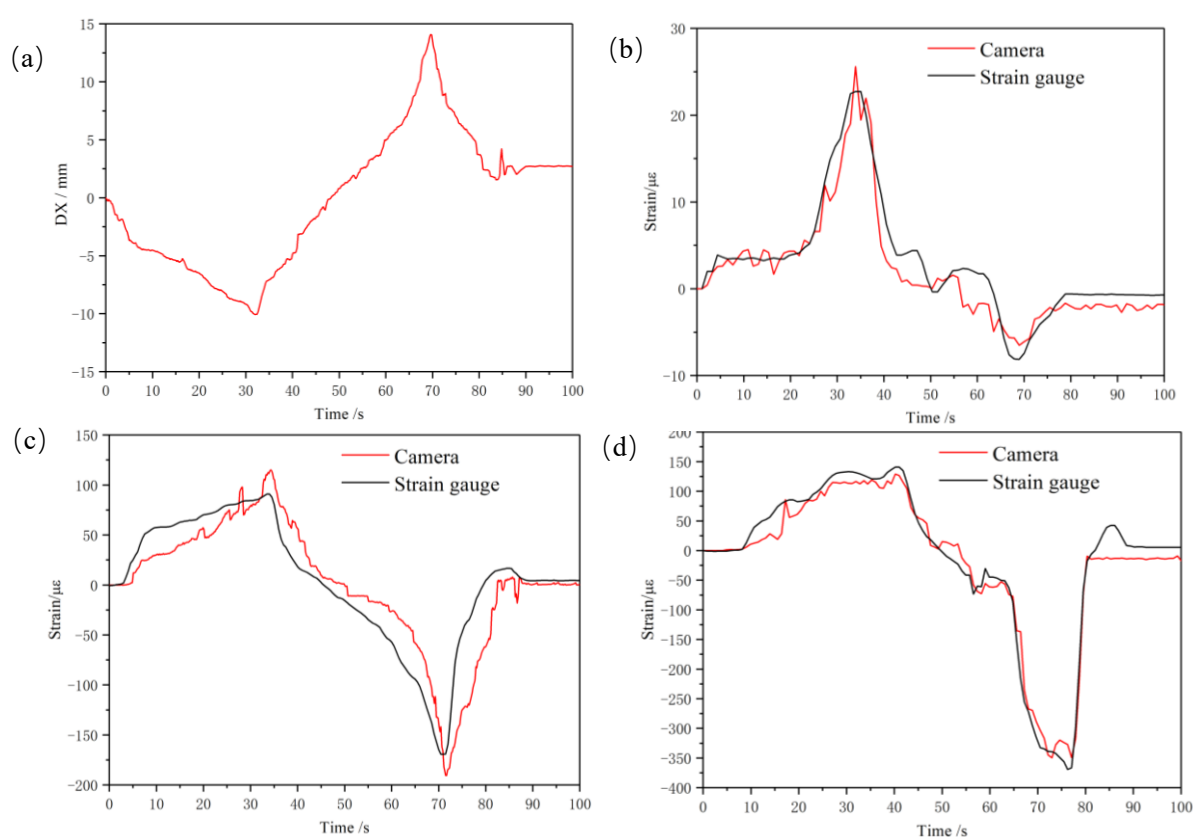
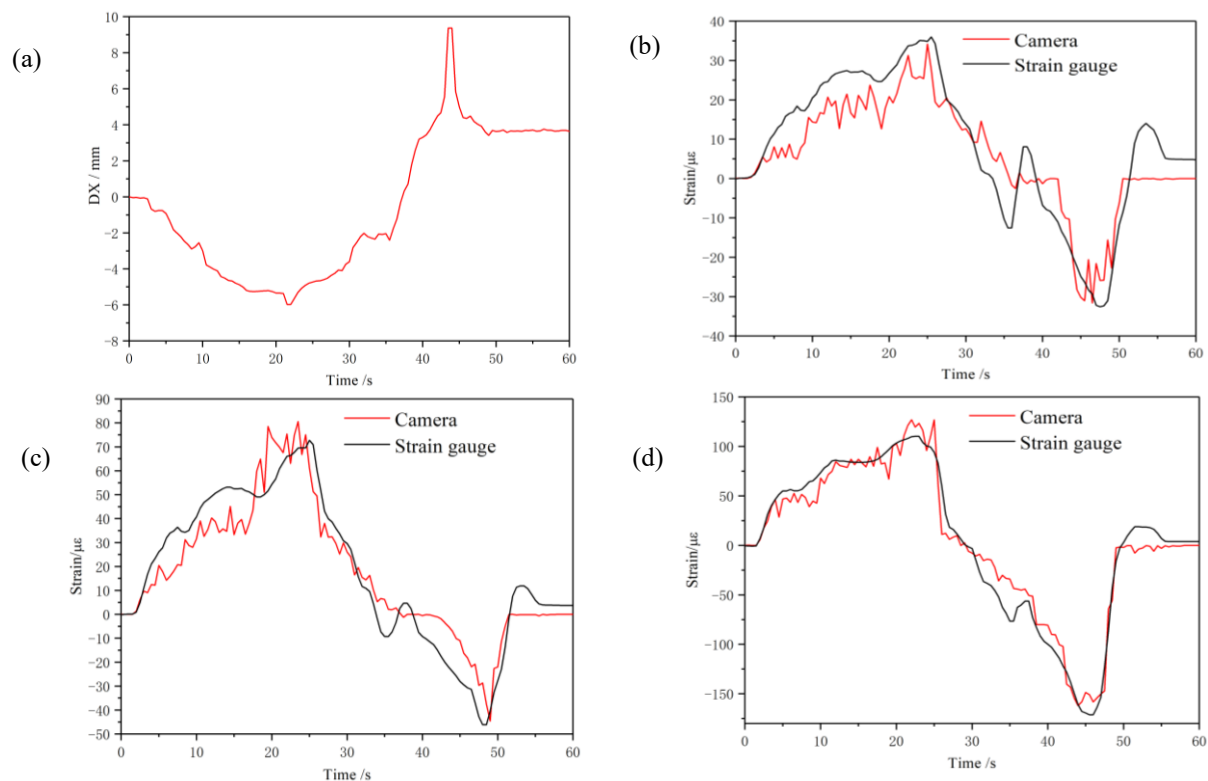


Fig. 10. Testing result of Case1

(a) Time-history curve of horizontal displacement of top pile; (b) Comparison result of average strain of strain gauge (4); (c) With strain gauge(5); (d)With strain gauge(6);



**Fig. 11.** Testing result of Case2

(a) time-history curve of horizontal displacement of top pile; (b) Comparison result of average strain of strain gauge (4); (c) with strain gauge(5); (d)with strain gauge(6);

## 5. Conclusions

In this study, the digital image method is used to make two contributions to the deformation measurement in the pile-soil load test. One is monitoring deformation field of soil around the pile based on DIC; the other is tracing the displacement and strain of the pile through an improved features tracing technology SURF-BRISK. Different from the existing literature, the concept of optical extensometer in optical mechanics was first applied in the strain measurement of non-uniform deformation steel pipe pile in this study, which broke through the limitation of the application of the optical extensometer to uniaxial tension. However, it can be seen from this paper that the accuracy

of the proposed optical method is not comparable to that of strain gauge. The main reasons are summarized as follows:

- (1) The surface features of pile body are not remarkable, reducing matching accuracy.
- (2) The tempered glass may interfere the image quality.
- (3) It is inevitable that the sand will come into the interaction surface of the pile and glass during the loading process, which will affect the marking points tracking.

However, the results obtained in this paper still show that the optical measurement is not nonsense in small strain measurement and solving the above problems is the focus of next research.

## Reference

- [1] Ghosh. B., Madabhushi.S.PQ. Centrifuge modelling of seismic soil structure interaction [J]. Nuclear Engineering and Design. 2007, 237(8): 887-896.
- [2] Li yuanhai, Zhu hehua, et al. Measurement of deformation field in sand model test based on image correlation analysis [J]. Journal of geotechnical engineering, 2004, 26 (1): 36. 41. (in Chinese)
- [3]White D J, Take W A & Bohon M D. Soil deformation measurement using particle image velocimetry (PIV) and photo Fammetry [J]. 2003, 53(7): 619—631.
- [4]Peters W H, Ranaon W F. Digital images Techniques in Experimental Mechanics [J].Opt.Eng.1982, 21(3): 427—431.

- [5] Tournonias.M., Bueno.M.A., Bigue.L, et al.. Contactless optical extensometer for textile materials [J].*Experimental Mechanics*, 2005, 45(5):420-426.
- [6] Zhang.D., Arola.D., Charalambides.P.G,et al.. On the mechanical behavior of carbon-carbon optic grids determined using a bi-axial optical extensometer [J].*Journal of Materials Science*, 2004, 39(14):4495-4505.
- [7] Kumap.K, Pooleery.A., Madhusoodanan.K., et al.. Optimisation of thickness of miniature tensile specimens for evaluation of mechanical properties [J].*Materials Science and Engineering: A*, 2016, 675:32-33.
- [8] Dubos P A, Fleurier G, Hugu. An experimental investigation of size effects in forming processes of high-purity thin metallic sheets [J].*materials Science Forum*, 2016, 879:459-464.
- [9]Wang W, He X Y. Application of optical extensometer on the real-strain measurement of low-dimensional materials [J]. *Acta Optica Sinica*, 2010, 30(6):1662-1666. (in Chinese)
- [10]Pan B, Yu LP, Wu DF. High-Accuracy 2D digital image correlation measurements with bilateral telecentric lenses: error analysis and experimental verification. *Exp Mech* 2013; 53(9):1719–33.
- [11] Helm JD, McNeill SR, Sutton MA. Improved three-dimensional image correlation for surface displacement measurement. *Opt Eng* 1996; 35(7):1911–20.
- [12] Luo PF, et al. Accurate measurement of three-dimensional deformations indeformable and rigid bodies using computer vision. *Exp Mech* 1993; 33(2):123–32.
- [13] Tsai RY. A versatile camera calibration technique for high-accuracy 3D machine vision metrology using off-the-shelf TV cameras and lenses. *IEEE J Robot Autom* 1987; 3(4):323–44.
- [14] Pengxiang Bai, Feipeng Zhu, Xiaoyuan He. Optical extensometer and elimination of the effect of out-of-plane motions. *Optics and Lasers in Engineering* 65 (2015) 28–37
- [15] Lowe, D.G.: Distinctive image features from scale-invariant keypoints. *Int. J.Comput. Vis.* 60(2), 91–110 (2004).
- [16] Rublee, E., Rabaud, V., Konolige, K., Bradski, G.: ORB: an efficient alternative to SIFT or SURF. In: 2011 IEEE International Conference on Computer Vision (ICCV), pp. 2564–2571, November 2011.
- [17] Leutenegger, S., Chli, M., Siegwart, R.Y.: BRISK: binary robust invariant scalable key points. In: 2011 IEEE International Conference on Computer Vision (ICCV), pp. 2548–2555. IEEE (2011).
- [18] Alahi, A., Ortiz, R., Vandergheynst, P.: FREAK: fast retina key point. In: IEEE Conference on Computer Vision and Pattern Recognition (2012).
- [19] SIFT and SURF Performance Evaluation and the Effect of FREAK Descriptor in the Context of Visual Odometry for Unmanned Aerial Vehicles.
- [20] BEKELE D, TEUTSCH M, SCHUCHERT T. Evaluation of binary key point descriptor [C] // IEEE International Conference on Image Processing. Melbourne, Australia: IEEE, 2013:3652-3656.
- [21]Zhang Z. A flexible new technique for camera calibration [J]. *Pattern Analysis and Machine Intelligence*, IEEE Transactions on, 2000, 22(11): 1330-1334.